ARL-TR-8885 ● JAN 2020

Multiobjective Optimization of Deflection and Curvature Radius in a Microelectromechanical System (MEMS) Bimorph Cantilever Actuator Driven by Shape Memory Alloy (SMA) Thin-Film Phase Change

by Cory R Knick, Han Zhou, Gaurav Kumar, and Paul Monaghan

NOTICES

Disclaimers

ARL-TR-8885 ● JAN 2020

Multiobjective Optimization of Deflection and Curvature Radius in a Microelectromechanical System (MEMS) Bimorph Cantilever Actuator Driven by Shape Memory Alloy (SMA) Thin-Film Phase Change

Cory R Knick
Sensors and Electron Devices Directorate, CCDC Army Research Laboratory

Han Zhou, Gaurav Kumar, and Paul Monaghan
University of Maryland, Mechanical Engineering Department

REPORT DOCUMENTATION PAGE	*Form Approved* *OMB No. 0704-0188*

1. REPORT DATE *(DD-MM-YYYY)*	2. REPORT TYPE	3. DATES COVERED (From - To)
January 2020	Technical Report	August 2019–December 2019

4. TITLE AND SUBTITLE	
Multiobjective Optimization of Deflection and Curvature Radius in a Microelectromechanical System (MEMS) Bimorph Cantilever Actuator Driven by Shape Memory Alloy (SMA) Thin-Film Phase Change	5a. CONTRACT NUMBER
	5b. GRANT NUMBER
	5c. PROGRAM ELEMENT NUMBER
6. AUTHOR(S)	5d. PROJECT NUMBER
Cory R Knick, Han Zhou, Gaurav Kumar, and Paul Monaghan	5e. TASK NUMBER
	5f. WORK UNIT NUMBER
7. PERFORMING ORGANIZATION NAME(S) AND ADDRESS(ES)	8. PERFORMING ORGANIZATION REPORT NUMBER
CCDC Army Research Laboratory ATTN: FCDD-RLS-RL Adelphi, MD 20783-1138	ARL-TR-8885
9. SPONSORING/MONITORING AGENCY NAME(S) AND ADDRESS(ES)	10. SPONSOR/MONITOR'S ACRONYM(S)
	11. SPONSOR/MONITOR'S REPORT NUMBER(S)

12. DISTRIBUTION/AVAILABILITY STATEMENT

Approved for public release; distribution is unlimited.

13. SUPPLEMENTARY NOTES

ORCID ID: Cory Knick, 0000-0002-3536-0722

14. ABSTRACT

At the microscale, shape memory alloy (SMA) microelectromechanical system (MEMS) bimorph actuators offer great potential based on their inherently high work density. An optimization problem relating to the deflection and curvature based on shape-memory MEMS bimorph was identified, formulated, and solved. Thicknesses of the SU-8 photoresist and nickel–titanium alloy (NiTi) were identified that yielded maximum deflections and curvature radius based on a relationship among individual layer thicknesses, elastic modulus, and cantilever length. This model should serve as a guideline for optimal NiTi and SU-8 thicknesses to drive large deflections and curvature radius that are most suitable for microrobotic actuation, micromirrors, micropumps, and microgrippers.

15. SUBJECT TERMS

shape memory alloy, microactuators, optimization, microelectromechanical system, MEMS, phase change

16. SECURITY CLASSIFICATION OF:			17. LIMITATION OF ABSTRACT	18. NUMBER OF PAGES	19a. NAME OF RESPONSIBLE PERSON
					Cory R Knick
a. REPORT	b. ABSTRACT	c. THIS PAGE	UU	39	19b. TELEPHONE NUMBER (Include area code)
Unclassified	Unclassified	Unclassified			(301) 394-1147

Standard Form 298 (Rev. 8/98)
Prescribed by ANSI Std. Z39.18

Contents

List of Figures

List of Tables

1. Introduction and Literature Review

1.1 Overview

In certain applications for microelectromechanical system (MEMS) microactuators, large deflections would be desired, such as the case of micro-robotics,[1–3] micromirrors,[4–6] and microgrippers.[3,7] A shape memory alloy (SMA), a material that undergoes large changes in stress during a temperature cycle due to a solid–solid-phase change, can be used to generate large, nonlinear deflections. We aim to find a relationship between deflections of a SMA MEMS actuator and maximize the deflection of SMA MEMS bimorph. SMA films based on sputtered nickel–titanium alloy (NiTi) have been exhaustively characterized in previous decades, leading to a wealth of information about the intricate interplay among NiTi ratio, annealing temperatures and times, and thickness.[8–31] Bimorphic actuators can impart reversible-deflection shape memory microactuators as previously demonstrated.[32,33] To date, optimization of parameters for improving shape-memory-induced actuation has not been explored. We chose for our candidate system an SU-8 patterned on top of NiTi SMA bimorph actuator. In this case, residual strains develop during the processing of MEMS actuators, and upon release from substrate the device curls upward to relieve these strains. Thermal input converts the material into austenite, and shape-memory effect drives the actuator into a flatter position, a process that is reversible upon subsequent thermal cycles. Thermal effects can be delivered to the SMA MEMS using laser irradiation[34] and joule-heating[35] at frequencies up to at least 1 kHz. SU-8, an epoxy-based photoresist, is an ideal material due to its relative ease of use in MEMS, low modulus of elasticity that enables more flexible devices with large deflection, and good chemical stability.

1.2 Background

Much literature exists for thin-film development and characterization of NiTi SMA.[1–4] Although many demonstrations of SMA MEMS actuators have been shown,[9,34–43] none of these citations perform design optimization studies to maximize deflection or curvature radius due to residual stress changes due to phase change. When the Nitinol is thermally cycled between martensite and austenite phases, there is a corresponding change in residual stress, which is used to drive the nonlinear deflections. This nonlinear and large change in stress is defined as the recovery stress and is a principal factor influencing the deflection and curvature radius. Our novel contributions take a realistic SMA MEMS bimorph design based on SU-8 on NiTi and determine optimal thickness combinations to yield maximized deflections, which would be desirable in certain applications where large strokes are desired. We feed into the model the Young's modulus values for NiTi thin films that have been determined previously using nanoindentation techniques.[44,45]

1.3 Building and Characterizing the SMA MEMS Actuators

The NiTi would be co-sputtered onto a 4-inch silicon (Si) wafer based on the methods reported in previous works.[8,34–36] The substrate is rotated and heated during deposition to ensure crystallization of the film. The wafer stress versus temperature measurements are performed, using Stoney's equation to determine recovery stress, hysteresis, and residual stress in the NiTi film. After verification of good SMA properties in the film at wafer level, a photomask is used to pattern bimorph actuator. Ion milling is used to remove portions of the NiTi film on the wafer. The SU-8 2000.5 is spin-coated (where the revolutions per minute are used to control SU-8 thickness) and another mask plate is used to pattern SU-8 on top of the NiTi cantilever. Finally, the device is released by etching the Si substrate away in xenon difluoride (XeF_2) gas. In practice, SU-8 thickness would be controlled by varying spin speed and NiTi thickness based on sputtering time.

2. Problem Definition and Formulation

2.1 Problem Identification

The design problem is to maximize the deflection of a MEMS bimorph cantilever beam based on the nonlinear SMA as the actuating mechanism. The deflection is dependent in large part on the parameter called recovery stress. The larger the recovery stress, the larger the deflection. We may also wish to decrease the overall mass or volume of the actuator or minimize the curvature radius. The objectives are competing in that reduction in the SMA thickness generally leads to reduction of the recovery stress. The bimorph actuator could consist of SU-8 on top of NiTi thin film, but this optimization model would be easily extensible to other cases of interest.

We should consider that the equation describing the recovery-stress-induced deflection in SMA MEMS actuator is Eq. 1.

Initially, the contour plots of SU-8 and NiTi thickness showed that the optimization problem was not interesting for the simplest case of constant recovery stress over the range of NiTi thickness. To our advantage, the NiTi recovery stress is a parameter that depends on NiTi thickness, which makes the optimization problem more interesting.

The equation describing the recovery-stress-induced deflection in SMA MEMS actuator is

$$d = \frac{3E_{NiTi}\sigma_{rec}t_{NiTi}t_{SU8}(t_{NiTi}+t_{SU8})l^2}{E_{NiTi}^2 t_{NiTi}^4 + E_{SU8}E_{NiTi}(4t_{NiTi}^3 t_{SU8} + 6t_{NiTi}^2 t_{SU8}^2 + 4t_{NiTi}t_{SU8}^3) + E_{SU8}^2 t_{SU8}^4} \quad (1)$$

where

σ_{rec} = recovery stress of the *SMA MEMS* actuator;

d = deflection of the *SMA MEMS* actuator;

l = total length of the *SMA MEMS* actuator;

E_{NiTi} = elastic modulus of *NiTi* layer;

E_{SU8} = elastic modulus of *SU-8* layer;

t_{NiTi} = thickness of *NiTi* layer;

t_{SU8} = thickness of *SU-8* layer.

Equation 1 comes from the textbook *MOEMS: Micro-opto-electro-mechanical Systems*[46] in the chapter on SMAs and its section on SMA bimorph.

Figure 1 shows stress versus temperature curves for NiTi on Si wafer for films deposited and characterized at the US Army Combat Capabilities Development Command Army Research Laboratory. These curves are experimentally generated and indicate the recovery stress (difference between highest and lowest stress values) and the thermal hysteresis. Here, as an illustrative example, the NiTi thickness is 900 nm, and the temperature cycle is performed using a heating and cooling rate of 1 °C/min.

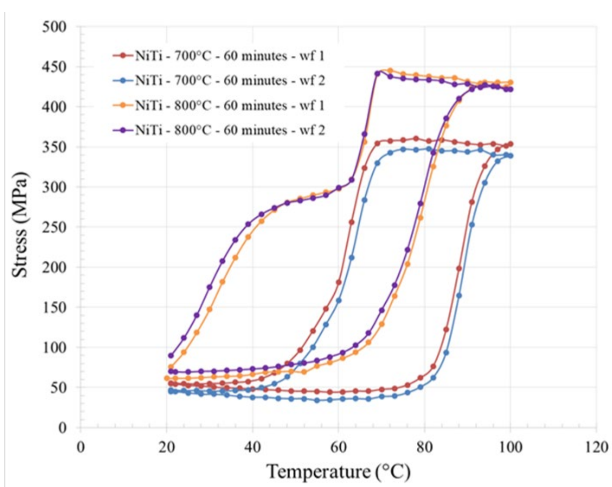

Fig. 1 Stress vs. temperature curves for NiTi on Si wafer are experimentally generated and indicate recovery stress (difference between highest and lowest stress values) and thermal hysteresis

2.2 Assumptions

We assume operating temperatures go between room temperature and 100 °C to ensure full phase change. In all calculations, for simplicity we use Young's modulus of NiTi as a fixed value. In reality, the Young's modulus changes during the phase change. Martensite (lower temperature phase) usually has a lower elastic modulus compared with the higher-temperature austenite phase.

Figure 2 shows the process used to build the SMA MEMS bimorph actuator comprising the NiTi SMA layer underneath the SU-8 elastic layer. In Step A there is deposition of SMA onto Si wafer and pattern using photolithography. In Step B, ion milling is performed to transfer the pattern into the SMA layer. In Step C, we spin on SU-8 and pattern it with mask plate and photolithography. In Step D, we release the MEMS bimorph by etching Si substrate with xenon difluoride (XeF_2) gas. And, in Step E we thermally actuate the two-way shape-memory MEMS device between curled and flat states.

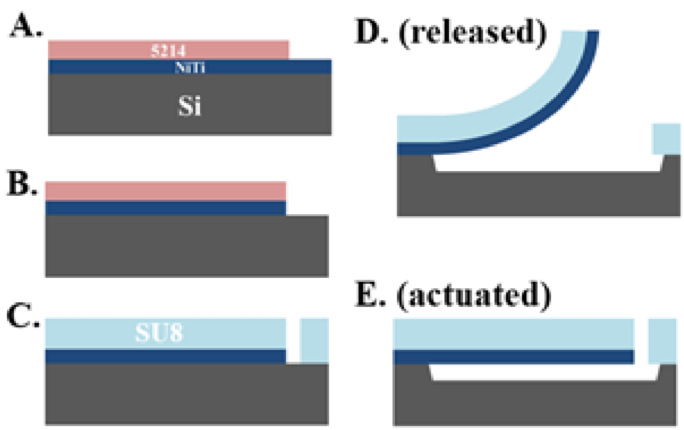

Fig. 2 SMA MEMS fabrication process for SU-8 on NiTi bimorph

3. Methods, Results, and Discussions

3.1 Single-Objective Optimization Problem

Based on literature review, we determined the recovery stress in thin films of NiTi deposited onto Si wafer depends upon the thickness of NiTi.[23]

3.1.1 Curve Fitting

Table 1 lists data from our literature review.

Table 1 Literature-review data

NiTi thickness (nm)	Recovery stress (MPa)
100	0
200	100
300	300
400	400
500	500
600	580
700	590
800	595
900	600
1000	570
1100	520
1200	500
1300	480
1400	460
1500	440
1600	430
1700	425
1800	420
1900	410
2000	400

Regarding NiTi recovery stress, there would appear to be an optimal thickness range for which recovery stress reaches maximum values, below which there is a sharp drop off. Therefore, the tendency for increased deflections for thinner materials reaches a point of diminishing returns due to the effect of decreasing recovery stress. Below 100–150 nm, shape-memory properties have been shown to drop off completely, so we impose constraints for NiTi thickness to vary between 150 and 1300 nm (Fig. 3).

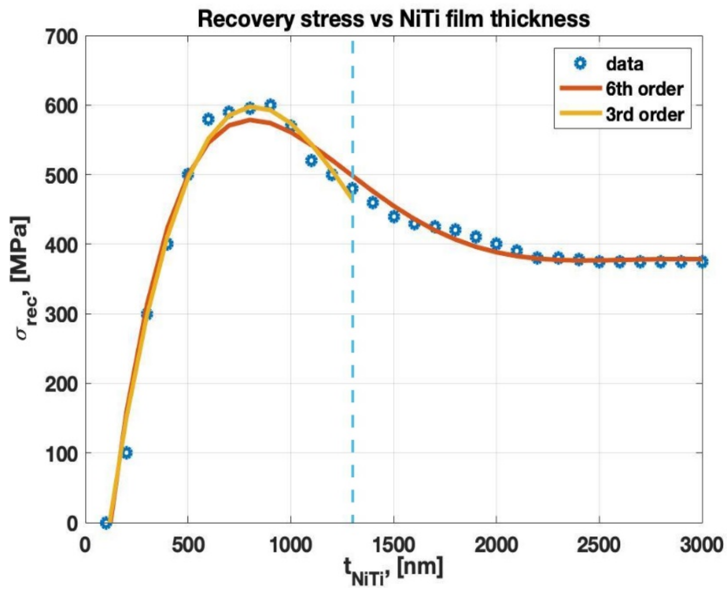

Fig. 3 Relation between recovery stress (MPa) and NiTi film thickness (nm)

There is a third-order polynomial curve fitting

$$y = 5.36E26x^3 - 2.15E21x^2 + 2.45E15x - 2.58E08. \tag{2}$$

Also, there is a sixth-order polynomial curve fitting

$$y = -5.11E42x^6 + 8.97E37x^5 - 6.22E32x^4 + 2.15E27x^3 - 3.82E21x^2 + 3.08E15x - 3.22E08 . \tag{3}$$

3.1.2 Problem Statement

Assume the elastic modulus of different layer as

$$E_{NiTi} = 30, 60, 80\ GPa$$

$$E_{SU8} = 2\ GPa$$

Based on the curve-fitting Eq. 2, the single-objective optimization problem can be written as following:

Maximize

$$d = \frac{3E_{NiTi}\sigma_{rec}t_{NiTi}t_{SU8}(t_{NiTi}+t_{SU8})l^2}{E_{NiTi}^2 t_{NiTi}^4 + E_{SU8}E_{NiTi}(4t_{NiTi}^3 t_{SU8} + 6t_{NiTi}^2 t_{SU8}^2 + 4t_{NiTi}t_{SU8}^3) + E_{SU8}^2 t_{SU8}^4}, \tag{4}$$

Subjected to

$$100\ \mu m \le l \le 300\ \mu m$$

$$150\ nm \le t_{NiTi} \le 1000\ nm$$

$$200\ nm \le t_{SU8} \le 2000\ nm$$

$$\sigma_{rec} \ge 0$$

$$\sigma_{rec} = 5.36E26 t_{NiTi}{}^3 - 2.15E21 t_{NiTi}{}^2 + 2.45E15 t_{NiTi} - 2.58E08\ (SI\ units)\ . \tag{5}$$

Covert to standard form in SI units:

Minimize

$$f = \frac{-3E_{NiTi}\sigma_{rec}t_{NiTi}t_{SU8}(t_{NiTi}+t_{SU8})l^2}{E_{NiTi}^2 t_{NiTi}^4 + E_{SU8}E_{NiTi}\left(4t_{NiTi}^3 t_{SU8} + 6t_{NiTi}^2 t_{SU8}^2 + 4t_{NiTi}t_{SU8}^3\right) + E_{SU8}^2 t_{SU8}^4} \tag{6}$$

Subjected to

$$g_1: 100 \times 10^{-6} - l \le 0;$$

$$g_2: l - 300 \times 10^{-6} \le 0;$$

$$g_3: 150 \times 10^{-9} - t_{NiTi} \le 0;$$

$$g_4: t_{NiTi} - 1300 \times 10^{-9} \le 0;$$

$$g_5: 200 \times 10^{-9} - t_{SU8} \le 0;$$

$$g_6: t_{SU8} - 2000 \times 10^{-9} \le 0;$$

$$g_7: -\sigma_{rec} \le 0$$

$$h_1: \sigma_{rec} - 5.36 \times 10^{26} t_{NiTi}{}^3 + 2.15 \times 10^{21} t_{NiTi}{}^2 - 2.45 \times 10^{15} t_{NiTi} + 2.58 \times 10^8 = 0 \tag{7}$$

3.2 MATLAB Optimization Toolbox (*fmincon*)

The corresponding MATLAB file is as follows:

1) MaxDeflection.m (fmincon function)
2) SingleObjectiveOptimization.m (optimization)
3) SingleObjectiveOptimization_ContourPlot_L300um.m (contour plot)

3.2.1 MATLAB Output

The variables are as follows:

$$t_{NiTi} = 385\ nm$$

$$t_{SU8} = 884\ nm$$

$$l = 300\ \mu m$$

$$\sigma_{rec} = 396\ MPa$$

The maximum deflection is

$$d = -f = 0.0081\ m$$

Figure 4 assumes the simplest scenario with constant recovery stress in the NiTi layer; however, the real optimization problem should consider the NiTi recovery-stress dependence on NiTi film thickness.

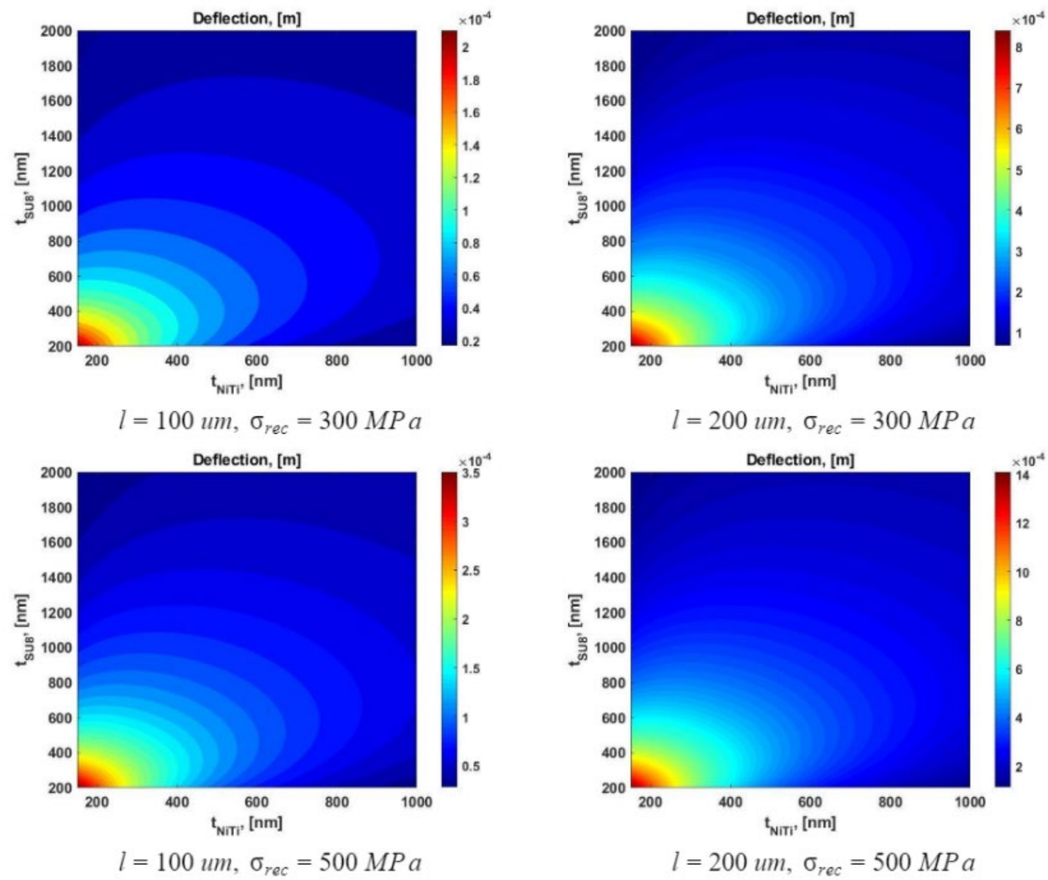

Fig. 4 Contour plots data showing the uninteresting optimization problem would be in the origin (thinnest possible values for each material in the bimorph film stack)

3.2.2 Optimal Solution

From experimental data, the recovery stress and NiTi film thickness have the following relationship, which was taken from published data relating recovery stress to NiTi thickness.[23] According to the MATLAB toolbox, the optimal solution is $t_{NiTi} = 359\ nm, t_{SU8} = 275\ nm, l = 300\ \mu m$. The optimization result is similar for the cases where we treat the elastic modulus of SU-8 as 2 and 3 GPa, which is more realistic with reported values from manufacturer (MicroChem Corp). This is depicted in Fig. 5.

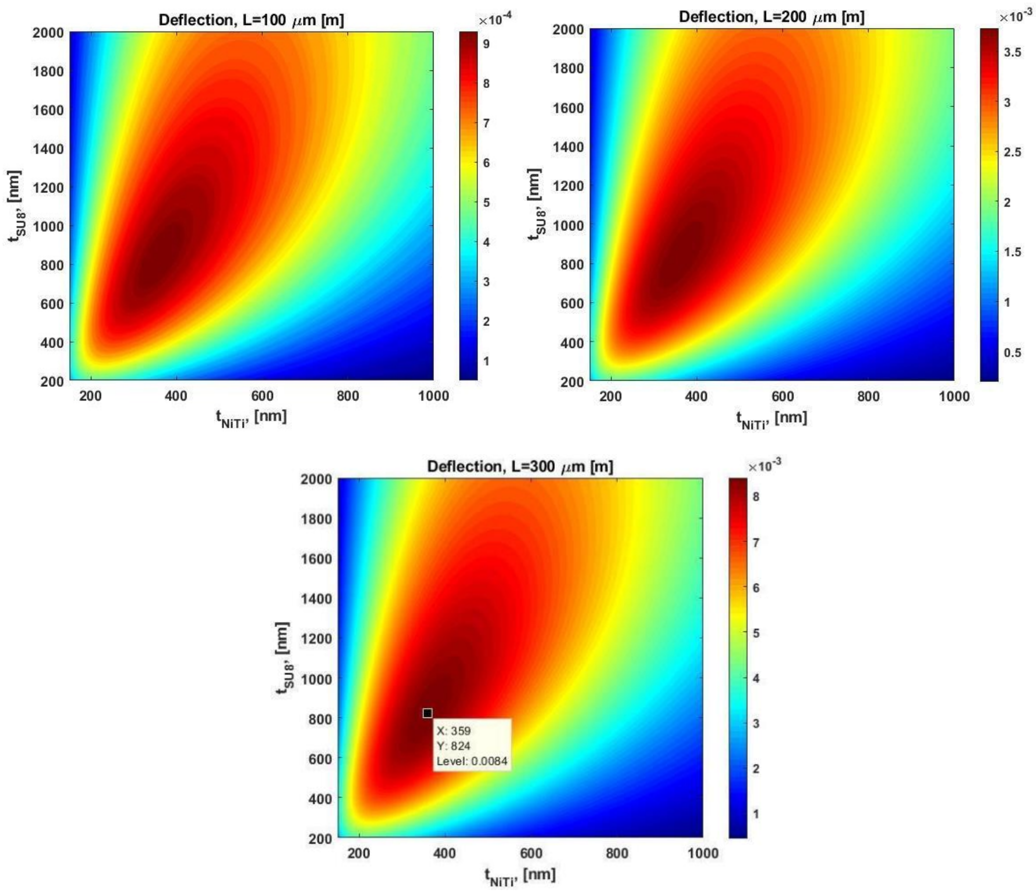

Fig. 5 Optimization contours for the case where the SU-8 elastic modulus is 2 GPa; variables considered are individual layer thicknesses: NiTi (x-axis) and SU-8 (y-axis)

According to the toolbox, the optimal solution is $t_{NiTi} = 359\ nm, t_{SU8} = 824\ nm, l = 300\ \mu m$.

3.3 Single-Objective Optimization (Excel Solver)

Excel Solver outputs the following results, which are consistent with the MATLAB *fmincon*:

Maximum deflection is d = –f = 0.0081 m

Optimized variables are as follows:

t_{NiTi} = 385 nm

$t_{SU\text{-}8}$ = 884 nm

L = 300 µm

σ_{rec} = 396 MPa

Figure 6 is a screenshot from the use of Excel Solver.

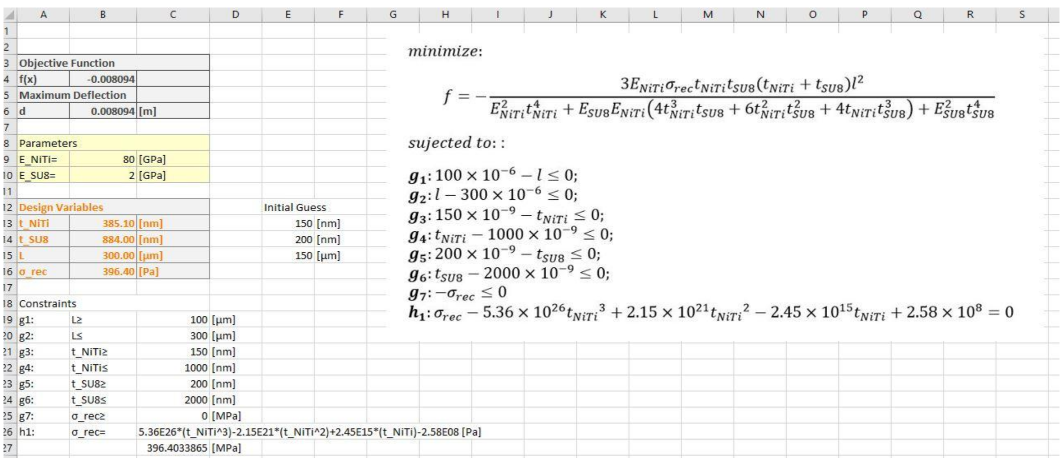

Fig. 6 Excel Solver results for single-objective optimization problem for maximize deflection

3.4 Multiobjective Optimization

3.4.1 Curvature-Radius Maximization

The curvature of a bilayer elastic material is given as[47]

$$K = \frac{-E'_{SU8}t_{SU8}E'_{NiTi}t_{NiTi}(t_{NiTi}+t_{SU8})}{G(E'_{SU8}t_{SU8}+E'_{NiTi}t_{NiTi})}\,\Delta\varepsilon, \tag{8}$$

$$G = E'_{SU8}t_{SU8}^2\left(\frac{t_{NiTi}}{2}-\frac{t_{SU8}}{6}-\theta\right) - E'_{NiTi}t_{NiTi}\left[\,t_{SU8}\left(t_{SU8}+\frac{t_{NiTi}}{2}\right)+\frac{t_{NiTi}^2}{6}+\theta(2t_{SU8}+t_{NiTi})\right], \tag{9}$$

$$\theta = \frac{t_{NiTi} t_{SU8} (E'_{NiTi} - E'_{SU8})}{2(E'_{SU8} t_{SU8} + E'_{NiTi} t_{NiTi})}, \quad (10)$$

and
$$\Delta\varepsilon = (\alpha_{SU8} - \alpha_{NiTi}) \Delta T. \quad (11)$$

where ρ is the curvature radius generally expressed in units of µm. $\Delta\varepsilon$ is a strain differential term resulting from CTE mismatch and temperature difference experienced during the processing. The θ is a correction factor used in the placement of neutral plane, while E' is the biaxial modulus defined as $\frac{E}{1-v}$ where v is Poisson's ratio and E is Young's modulus. Poisson ratios are assumed to be 0.22 for SU-8 and 0.33 for NiTi. The α_{SU8} is reported to be $52*10^{-6}$/°C. The α_{NiTi} (depending on austenite or martensite phase) is reported to be 6.6 or $11*10^{-6}$/°C. For simplicity sake, we assume an intermediate value of $\alpha_{NiTi} = 9*10^{-6}$/°C. Units for theta term are nm or m. Units for G term are Pa*nm^3 or Pa*m^3. Therefore, units for curvature are in nm or m. The $\Delta\varepsilon$ term is unitless.

The objective Number 2 is to maximize curvature radius. We determine the pareto frontier and strong pareto points using the epsilon constrained method. In this epsilon constrained method, we minimize f1 while keeping f2 less than or equal to different values of epsilon.

As a first step for objective Function 2 (curvature of bimorph) we coded MATLAB script to generate contour plots as a function of the two main design variables; that is, thickness of NiTi and SU-8. (This MATLAB code is in the Appendix.) The problem formulation for objective Function 2 is as follows.

Curvature is

$$K = -\frac{E'_{SU8} t_{SU8} E'_{NiTi} t_{NiTi} (t_{NiTi} + t_{SU8})}{G(E'_{SU8} t_{SU8} + E'_{NiTi} t_{NiTi})} \Delta\varepsilon. \quad (12)$$

Maximize

$$\rho = \frac{1}{K} = -\frac{G(E'_{SU8} t_{SU8} + E'_{NiTi} t_{NiTi})}{E'_{SU8} t_{SU8} E'_{NiTi} t_{NiTi} (t_{NiTi} + t_{SU8}) \Delta\varepsilon} \quad (13)$$

Subjected to

g1: $150 \times 10^{-9} - t_{NiTi} \leq 0$;

g2: $t_{NiTi} - 1300 \times 10^{-9} \leq 0$;

g3: $200 \times 10^{-9} - t_{SU8} \leq 0$;

g4: $t_{SU8} - 2000 \times 10^{-9} \leq 0$;

h1: $G - E'_{SU8}t_{SU8}^2\left(\frac{t_{NiTi}}{2} - \frac{t_{SU8}}{6} - \theta\right) - E'_{NiTi}t_{NiTi}\left[t_{SU8}\left(t_{SU8} + \frac{t_{NiTi}}{2}\right) + \frac{t_{NiTi}^2}{6} + \theta(2t_{SU8} + t_{NiTi})\right] = 0$

h2: $\theta - \frac{t_{NiTi}t_{SU8}(E'_{NiTi} - E'_{SU8})}{2(E'_{SU8}t_{SU8} + E'_{NiTi}t_{NiTi})} = 0$

3.4.1.1 MATLAB Output

The variables are as follows:

$$t_{NiTi} = 1300\ nm$$

$$t_{SU8} = 200\ nm$$

The maximum radius curvature (i.e., flattest beam) is

$$\rho_{max} = 0.0145m$$

Figure 7 depicts a MATLAB-generated contour plot of curvature radius (in meters) against the primary design variables (i.e., t_{NiTi} and t_{SU-8}). Curvature radius is maximized for the thickest values of NiTi and thinnest values of SU-8. The result is intuitive because this is the stiffest beam (from the perspective of thickest NiTi with much larger Young's modulus compared with SU-8). Thinner Su-8 means the effect from strain differential and CTE mismatch is minimized and contributes less to curvature radius; overall, this means the upper bound on NiTi thickness and lower bound on Su-8 thickness are active constraints for objective Function 2.

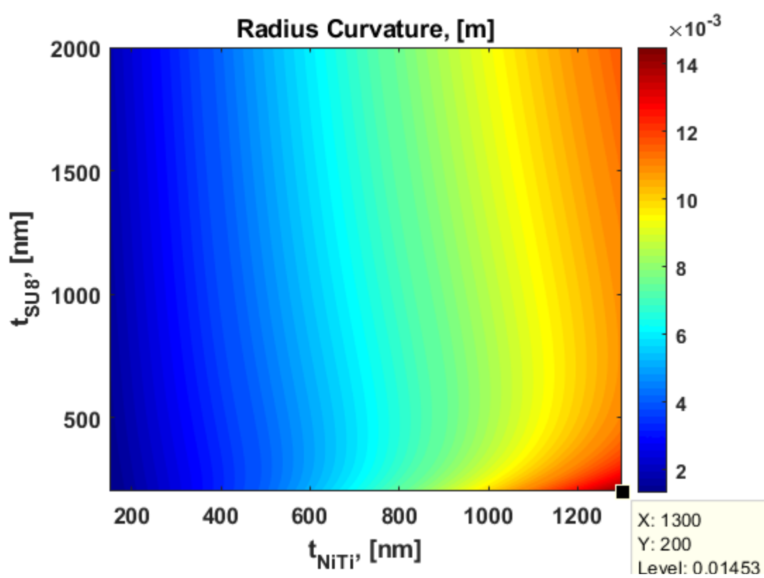

Fig. 7 MATLAB-generated contour plot of curvature radius against primary design variables t_{NiTi} and t_{SU-8}; curvature radius is maximized for the thickest values of NiTi and thinnest values of SU-8

For multiobjective optimization, the deflection and curvature radius of *SMA* bimorph actuator are maximized simultaneously. So, the multiobjective optimization problem can be stated as follows:

Maximize

f1: $\rho = -\frac{G(E'_{SU8}t_{SU8}+E'_{NiTi}t_{NiTi})}{E'_{SU8}t_{SU8}E'_{NiTi}t_{NiTi}(t_{NiTi}+t_{SU8})\Delta\varepsilon}$

f2: $d = \frac{3E_{NiTi}\sigma_{rec}t_{NiTi}t_{SU8}(t_{NiTi}+t_{SU8})l^2}{E_{NiTi}^2 t_{NiTi}^4+E_{SU8}E_{NiTi}(4t_{NiTi}^3 t_{SU8}+6t_{NiTi}^2 t_{SU8}^2+4t_{NiTi}t_{SU8}^3)+E_{SU8}^2 t_{SU8}^4}$

Subjected to

g1: $100 \times 10^{-6} - l \leq 0;$

g2: $l - 300 \times 10^{-6} \leq 0;$

g3: $150 \times 10^{-9} - t_{NiTi} \leq 0;$

g4: $t_{NiTi} - 1300 \times 10^{-9} \leq 0;$

g5: $200 \times 10^{-9} - t_{SU8} \leq 0;$

g6: $t_{SU8} - 2000 \times 10^{-9} \leq 0;$

g7: $-\sigma_{rec} \leq 0;$

h1: $\sigma_{rec} - 5.36 \times 10^{26} t_{NiTi}{}^3 + 2.15 \times 10^{21} t_{NiTi}{}^2 - 2.45 \times 10^{15} t_{NiTi} + 2.58 \times 10^8 = 0;$

h2: $G - E'_{SU8}t_{SU8}^2\left(\frac{t_{NiTi}}{2} - \frac{t_{SU8}}{6} - \theta\right) - E'_{NiTi}t_{NiTi}\left[t_{SU8}\left(t_{SU8} + \frac{t_{NiTi}}{2}\right) + \frac{t_{NiTi}^2}{6} + \theta(2t_{SU8} + t_{NiTi})\right] = 0;$

h3: $\theta - \frac{t_{NiTi}t_{SU8}(E'_{NiTi}-E'_{SU8})}{2(E'_{SU8}t_{SU8}+E'_{NiTi}t_{NiTi})} = 0.$

3.4.1.2 Two Functions in Conflict

Due to the conflicting nature of the two objective functions, the contour plot for the multiobjective function has changed substantially. Maximizing the radius is favored by a larger t_NiTi as opposed to a smaller thickness required to maximize deflection. The optimal solution of multiobjective function has a larger t_NiTi, as depicted in Fig. 8.

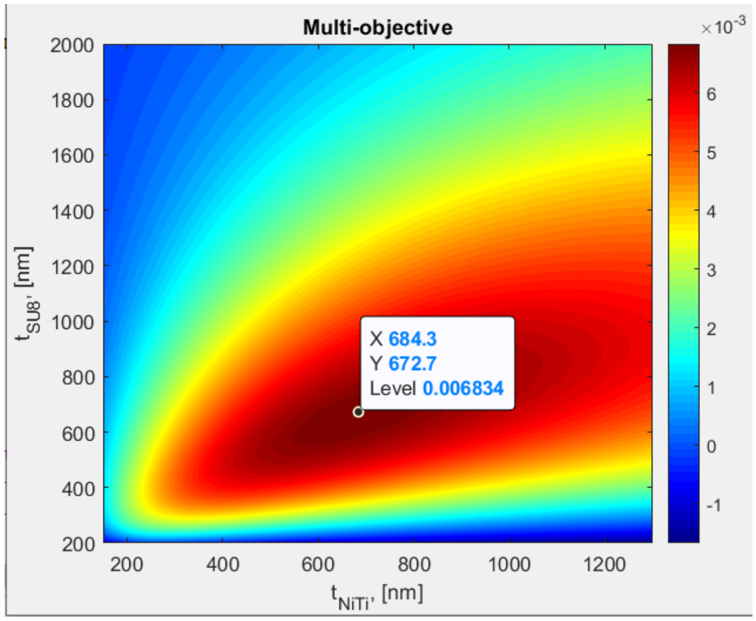

Fig. 8 Optimal solution for multiobjective optimization

To determine the Pareto frontier of the multiobjective optimization problem required all of the previously stated equality constraints to be substituted into the objective functions in terms of t_{NiTi} and t_{SU8}. Thus, the feasible decision space is a rectangular area for the lower and upper limits of NiTi and SU-8 layer thickness, shown in Fig. 9a. From previous single-objective optimization, the maximum deflection of the bimorph actuator occurred with a maximum length of the bimorph, where $l = 300$ µm. Based on the maximum bimorph length, the feasible objective space is shown in Fig. 9b, which is used for validation of our optimization solution.

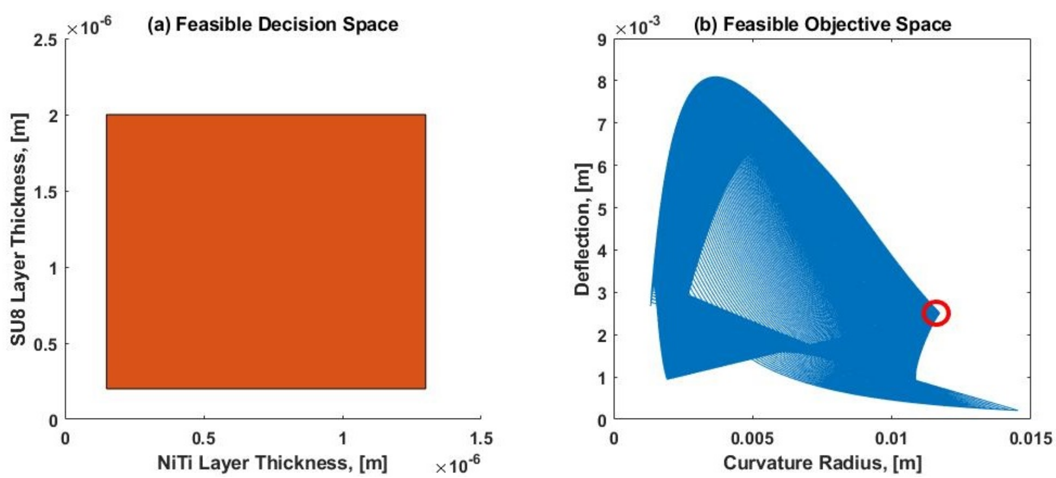

Fig. 9 Feasible decision space and objective space for multiobjective optimization

3.4.2 ε-Constraint Method

For this section, the ε-constraint method is used to determine the Pareto frontier of our multiobjective optimization problem. The first objective function is kept, which is the maximization of the bimorph deflection, and the second objective function is restricted with different ε value, which is the curvature radius of the bimorph. Accordingly, the multiobjective optimization problem is converted to the following form:

Maximize

$$f_2: d = \frac{3E_{NiTi}\sigma_{rec}t_{NiTi}t_{SU8}(t_{NiTi}+t_{SU8})l^2}{E_{NiTi}^2 t_{NiTi}^4 + E_{SU8}E_{NiTi}(4t_{NiTi}^3 t_{SU8} + 6t_{NiTi}^2 t_{SU8}^2 + 4t_{NiTi}t_{SU8}^3) + E_{SU8}^2 t_{SU8}^4}$$

Subjected to

$$f_1: \rho = -\frac{G(E'_{SU8}t_{SU8}+E'_{NiTi}t_{NiTi})}{E'_{SU8}t_{SU8}E'_{NiTi}t_{NiTi}(t_{NiTi}+t_{SU8})\Delta\varepsilon} \geq \varepsilon$$

$$\boldsymbol{g_j}(\boldsymbol{x}) \leq 0, \ \ j = 1,2,\dots,7$$

$$\boldsymbol{h_k}(\boldsymbol{x}) \leq 0, \ \ k = 1,2,3$$

Figure 10 shows the solution of maximum bimorph deflection with different ε value that rectricts the minimum value of bimorph radius curvature. By changing the lower limit for bimorph curvature, a series of solution is shown in Fig. 9 with two different termination conditions of MATLAB *fmincon* function. The blue-mark data points represent the valid solution, where local minimum was found and all constraints were satisfied. The red-mark data points are the invalid solution because *fmincon* function converged to an infeasible point. To validate our solution by using ε-constraint method, all solutions are plotted in feasible decision space as shown in Fig. 11, where the result perfectly matches the Pareto frontier of feasible decision space.

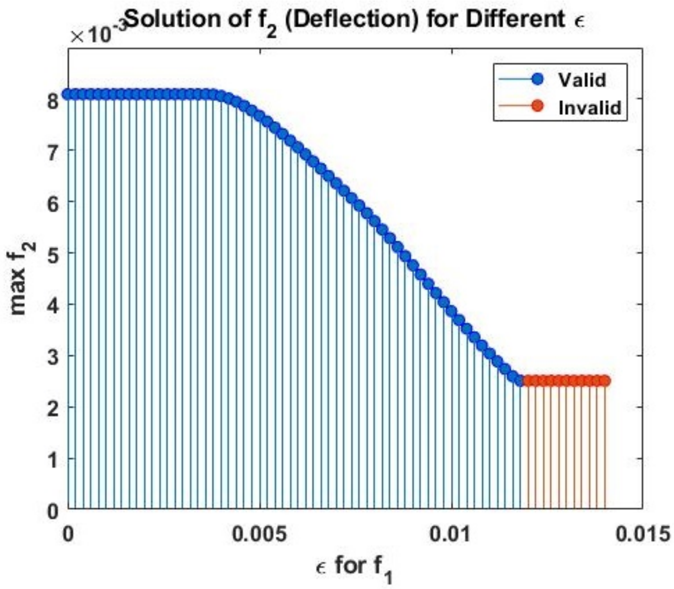

Fig. 10 Solution of maximum bimorph deflection with different ε values for f_1

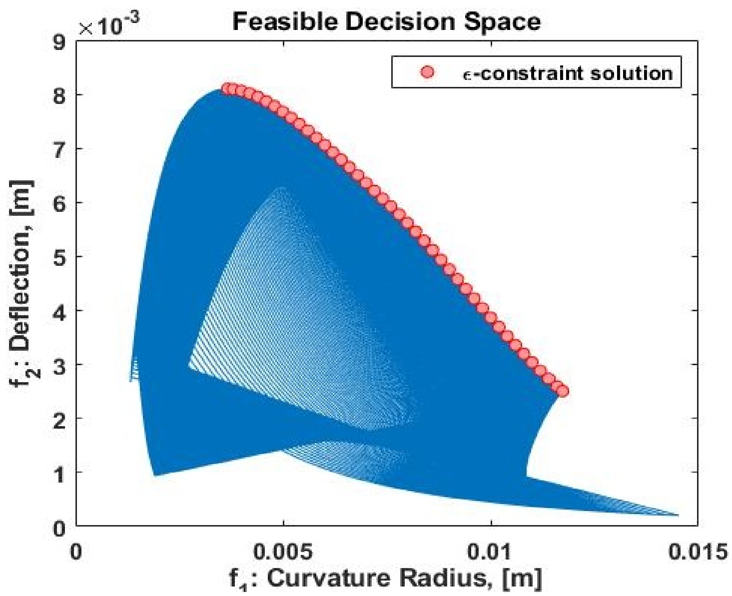

Fig. 11 ε-constraint solution in feasible decision space

3.4.3 Exterior Penalty Method

We wrote a MATLAB code for exterior penalty method to solve our optimization problem. The objective function is the one formulated for maximize deflection (yellow), followed by the penalty on violating the constraints that is highlighted in gray.

```
f1 = @(x) ((3*E_NiTi*x(4)*x(1)*x(2)*(x(1)+x(2))*x(3)^2)/
...(E_NiTi^2*x(1)^4+E_SU8*E_NiTi*(4*x(1)^3*x(2)+6*x(1)^2*
x(2)^2+4*x(1)*x(2)^3)+E_SU8^2*x(2)^4)...
+ 1e-5*rp1*((1e-16*(x(4)-5.36e26*x(1)^3+2.15e21*x(1)^2-
2.45e15*x(1)+2.58e8))^2 + 1e19*(max(0,-x(1)+150e-9))^2+
1e14*(max(0,-x(2)+200e-9))^2+ 1e8*(max(0,-x(3)+50e-
6))^2+...
1e14*(max(0,x(1)-1300e-9))^2 + 1e14*(max(0,x(2)-2000e-
9))^2 + 1e8*(max(0,x(3)-300e-6))^2));
```

We used an overall scaling factor of $1e^{-5}$ on the constraint violation, which is highlighted in blue, as well as using individual scaling factors for all of the constraints, which are highlighted in green. This was done to ensure the magnitude of all the constraint quantities are the same and that the magnitude of the constraint violation is of the same order as the objective function. We chose a value of 1.1 for gamma. And, finally, the optimal solution was t_{NiTi} = 150 nm, t_{SU-8} = 872 nm, and l = 300 µm. We observed that t_{NiTi} remains 150 nm, which is the lower bound. This happened because without the constraints, the objective function is strongly favored by a lower value of t_{NiTi}. Similarly, we observe the deflection monotonically increases with the length of the bimorph and therefore the optimal solution is L = 300 µm, which is the upper bound on L. We also compared our results by solving this optimization problem using *fmincon* in MATLAB and the results we thus obtained were very similar.

In order to choose appropriate scaling factors for the two functions and understand which points are dominant or dominated on the Pareto chart, we plotted the pareto chart (Fig. 12). First, we plotted the Pareto chart by using different values of weights and then optimizing the multiobjective function and accordingly plotting the individual objective functions. We also used the epsilon method to plot the Pareto frontier. From the Pareto chart, we identified the good and bad values for the objective functions and chose w = 0.5 as the raw data point. Using this, we calculated scaling factor for each objective function, which we found are

$$f_{scale,radius} = \frac{(236.5 - 297{,}02)}{(236.5 - 308.6)} = 0.8395 \quad (14)$$

$$f_{scale,deflection} = \frac{(0.0044 - 0.004609)}{(0.001523 - 0.004609)} = 0.0677 \quad (15)$$

Using the new scaling factors, we reevaluated the optimal solution using the penalty method and the result we obtained is slightly different; that is, we see an increase in t_{SU-8} thickness that favors optimization of radius of curvature.

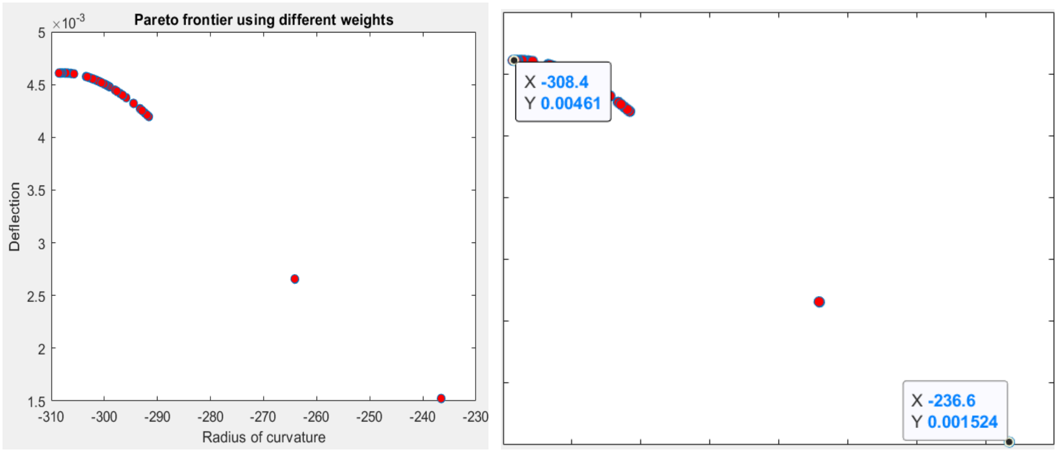

Fig. 12 Pareto frontier plots using the weighting method

4. Parametric Study

According to project requirements, once we have established the optimal objective values for deflection and curvature, we perform a sensitivity analysis of the following variables, which experimentally could be varied with relative ease. These thickness values, x1 and x2, corresponding to the NiTi and SU-8 thicknesses, can be changed by varying the spin speed for Su-8 coating: faster spins corresponding to thinner films of SU-8 and vice versa. For NiTi, longer sputter time would be used for thicker films and vice versa. Young's modulus can be varied by deposition conditions for NiTi and curing/baking temperatures and conditions for SU-8.

4.1 Sensitivity Analysis

To perform the sensitivity analysis for Objective 1, we keep fixed the optimal thickness for SU-8 and vary the NiTi thickness to see how it changes and plot a function and generate a table of values. Similarly, we keep fixed the optimal value of NiTi thickness and recovery stress and plot the deflection over a range of SU-8 thicknesses, as depicted in Fig. 13. Table 2 lists the various parameters for optimal solutions.

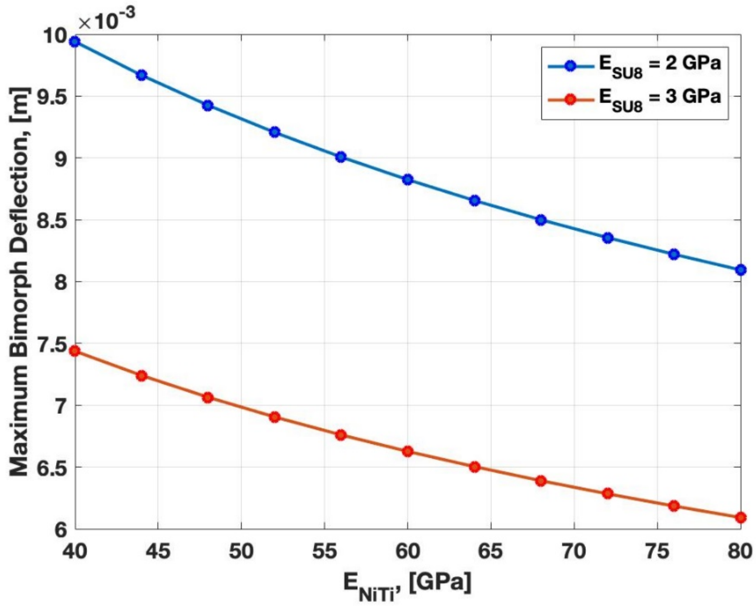

Fig. 13 Maximum bimorph deflection with variation of Young's modulus of NiTi and SU-8 layer

Table 2 Optimal solution by changing the value of parameters

Parameters		Optimal Solutions				
E_{NiTi}, GPa	E_{SU8}, GPa	T_{NiTi}, nm	T_{SU8}, nm	L, um	σ_{rec}, MPa	max d, m
40	**2**	385	675	300	396	0.0099
40	**3**	385	574	300	396	0.0074
60	**2**	385	791	300	396	0.0088
60	**3**	385	675	300	396	0.0066
80	**2**	385	884	300	396	0.0081
80	**3**	385	756	300	396	0.0061

Figure 14 depicts an animated sequence from the sensitivity analysis, which determines that as NiTi thickness increases, deflection decreases.

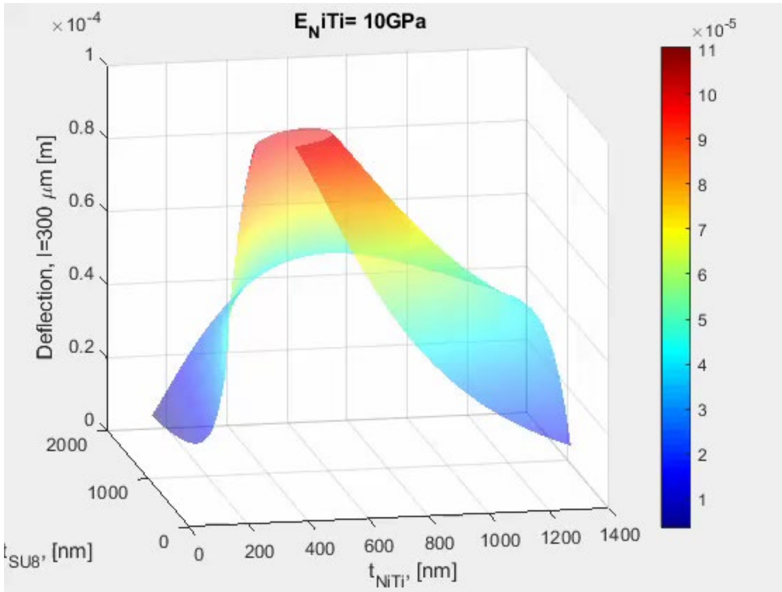

Fig. 14 Animated sequence (i.e., sensitivity analysis) of optimal solution while variations in NiTi thickness are made; deflection decreases as NiTi thickness increases

4.2 Robustness Analysis

During our analysis of results, we also observed that changing the starting point in the code (i.e., initial value of the variables) can result in a different optimal solution. This is primarily due to the highly nonlinear nature of the objective function. Therefore, to test the robustness of our code we generated of grid of multiple start points and performed an optimization with each starting point. The plot on the left of Fig. 15 shows how the optimal solution changes with each change in NiTi thickness. We observe a relatively flat curve that shows the optimal solution is not very sensitive to the change in starting point; however, we do notice certain starting points can change the optimal solution significantly. On the right of Fig. 15, we show a contour plot of the optimal solution while varying initial values of NiTi thickness and SU-8 thickness. And again, we observe that most of the plot is blue in color—showing little difference—but we do observe certain red bands where the optimal solution is substantially different.

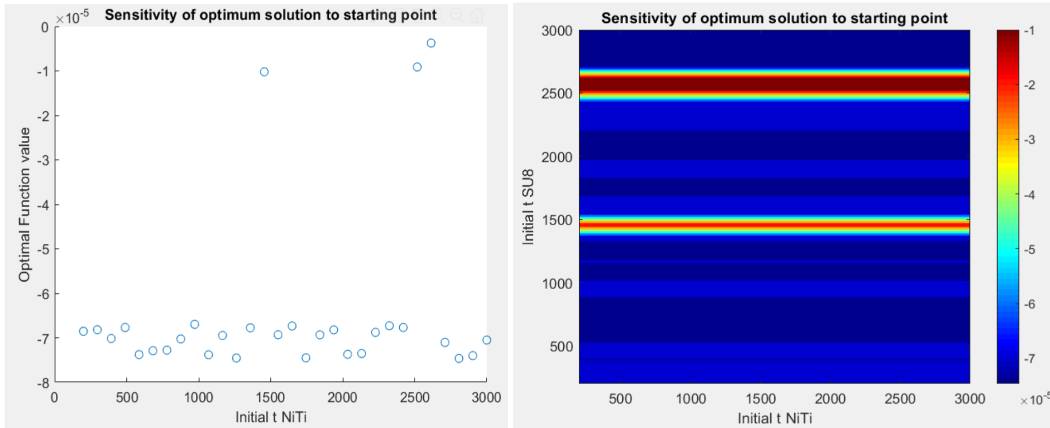

Fig. 15 Robustness analsysis for optimal solution: (left) with regard to NiTi thickness and (right) regarding NiTi and SU-8 thickness

5. Conclusion

An interesting optimization problem was identified whereby the deflection of shape-memory MEMS bimorph actuator was maximized. Original calculations showed reductions in thickness of the bimorph layers would yield maximized deflections (for the simplest case assuming constant values of recovery stress in NiTi layer). In the literature, a more complex relationship among recovery stress and the NiTi thickness was identified. A curve fit to these data yielded a much more interesting optimization problem that was solved graphically (contour plots) and using the Optimization Toolbox in MATLAB. Optimal NiTi and SU-8 thicknesses for the case where the SU-8 modulus was 2 GPa were determined to be $t_{NiTi} = 359\ nm, t_{SU8} = 824\ nm$. After solving the single-objective optimization problem using *fmincon*, Excel solver, and a hand-coded algorithm, we formulated a second objective function to maximize curvature radius (i.e., maximize the flatness of the beam because larger curvature radius is a flatter beam). We used *fmincon* to solve for the optimal values of NiTi and SU-8 to maximize curvature radius. We determined that the objective functions were conflicting—there was clearly a tradeoff in order to satisfy both conditions simultaneously—and therefore suitable for multiobjective optimization. We formulated a multiobjective optimization method and solved it using *fmincon*. Finally a parametric study or sensitivity analysis was performed pertaining to NiTi and SU-8 Young's modulus.

6. References

1. Lee HT, Kim MS, Lee GY, Kim CS, Ahn SH. Shape memory alloy (SMA)-based microscale actuators with 60% deformation rate and 1.6 kHz actuation speed. Small. 2018;14:e1801023.
2. Liu K, Cheng C, Cheng Z, Wang K, Ramesh R, Wu J. Giant-amplitude, high-work density microactuators with phase transition activated nanolayer bimorphs. Nano Lett. 2012;12:6302–6308.
3. Leong TG, Randall CL, Benson BR, Bassik N, Stern GM, Gracias DH. Tetherless thermobiochemically actuated microgrippers. Proc Natl Acad Sci USA. 2009;106:703–708.
4. Zanardi Ocampo JM, Vaccaro PO, Fleischmann T, Wang TS, Kubota K, Aida T, Ohnishi T, Sugimura A, Izumoto R, Hosoda M, et al. Optical actuation of micromirrors fabricated by the micro-origami technique. Appl Phys Lett. 2003;83(18):3647–3649.
5. Ritt G, Eberle B. Automatic laser glare suppression in electro-optical sensors. Sensors. 2015;15:792–802.
6. Goodwin SH, Dausch DE, Solomon SL, Lamvik MK. Electrostatic artificial eyelid actuator as an analog micromirror device. Proc SPIE. 2005;5785(1):59–67.
7. Malachowski K, Jamal M, Jin Q, Polat B, Morris CJ, Gracias DH. Self-folding single cell grippers. Nano Lett. 2014;14:4164–4170.
8. Ainslie K, Knick C, Smith G, Li J, Troxel C, Mehta A, Kukreja R. Controlling shape memory effects in NiTi thin films grown on Ru seed layer. Sens Act A: Phy. 2019;294:133–139.
9. Choudhary N, Kaur D. Shape memory alloy thin films and heterostructures for MEMS applications: a review. Sens Act A: Phy. 2016;242:162–181.
10. Kotnur VG, Tichelaar FD, Fu WT, De Hosson JTM, Janssen GCAM. Shape memory NiTi thin films deposited on polyimide at low temperature. Surf Coat Tech. 2014;258:1145–1151.
11. Sanjabi S, Sadrnezhaad SK, Barber ZH. Sputter alloying of Ni, Ti and Hf for fabrication of high temperature shape memory thin films. Mat Sci Tech. 2013;23:987–991.

12. Koker MKA, Schaab J, Zotov N, Mittemeijer EJ. X-ray diffraction study of the reverse martensitic transformation in NiTi shape memory thin films. Thin Sol Films. 2013;545:71–80.

13. König D, Buenconsejo PJS, Grochla D, Hamann S, Pfetzing-Micklich J, Ludwig A. Thickness-dependence of the B2–B19 martensitic transformation in nanoscale shape memory alloy thin films: zero-hysteresis in 75nm thick Ti51Ni38Cu11 thin films. Acta Materialia. 2012;60:306–313.

14. Chung CY, Chan PM. NiTi shape memory alloy thin film micro-cantilevers array. Thin Sol Films. 2011;519:5307–5309.

15. Annadurai A, Manivel Raja M, Prabahar K, Kumar A, Kannan MD, Jayakumar S. Stress analysis, structure and magnetic properties of sputter deposited Ni–Mn–Ga ferromagnetic shape memory thin films. J Magnet Mat. 2011;323:2797–2801.

16. Satoh G, Birnbaum A, Yao YL. Annealing effect on the shape memory properties of amorphous NiTi thin films. J Man Sci Eng. 2010;132(5):051004-1–051004-9.

17. Rao J, Roberts T, Lawson K, Nicholls J. Nickel titanium and nickel titanium hafnium shape memory alloy thin films. Surf Coat Tech. 2010;204:2331–2336.

18. Mandepudi S, Ackler H. Processing and characterization of composite shape memory alloy (SMA) thin film structures for microactuators. Proc SPIE. 2010;7644;76440N-1–76440N-12.

19. Martins RMS, Schell N, Reuther H, Pereira L, Mahesh KK, Silva RJC, Braz Fernandes FM. Texture development, microstructure and phase transformation characteristics of sputtered Ni–Ti shape memory alloy films grown on TiN<111>. Thin Sol Films. 2010;519(1):122–128.

20. Sanjabi S, Barber ZH. The effect of film composition on the structure and mechanical properties of NiTi shape memory thin films. Surf Coat Tech. 2010;204:1299–1304.

21. Wang X. Crystallization and martensitic transformation behavior of NiTi shape memory alloy thin films [dissertation]. [Cambridge (MA)]: Harvard University; 2007.

22. Wibowo E, Kwok CY. Fabrication and characterization of sputtered NiTi shape memory thin films. J Micromech Microeng. 2006;16:101–108.

23. Fu YQ, Zhang S, Wu MJ, Huang WM, Du HJ, Luo JK, Flewitt AJ, Milne WI. On the lower thickness boundary of sputtered TiNi films for shape memory application. Thin Sol Films. 2006;515(1):80–86.

24. Tomozawa M, Young Kim H, Miyazaki S. Microactuators using r-phase transformation of sputter-deposited Ti-47.3Ni shape memory alloy thin films. J Intel Mat Sys Struc. 2006;17.

25. Getchel DJ, Savage RN. Fabrication and composition control of NiTi shape memory thin films for microactuators. Mater Res Soc Symp Proc. 2005;875.

26. Ishida A, Sato M, Tabata O, Yoshikawa W. Shape memory thin films formed with carrousel-type magnetron sputtering apparatus. Smart Mat Struc. 2005;14:S216–S222.

27. Liu YS, Xu D, Jiang BH, Yuan ZY, Houtte PV. The effect of crystallizing procedure on microstructure and characteristics of sputter-deposited TiNi shape memory thin films. J Micromech Microeng. 2005;15:575–579.

28. Ho KK, Carman GP, Jardine PA, inventors. Bimorphic, compositionally-graded, sputter-deposited, thin film shape memory alloy. United States patent US6689486B2. 2004 Feb 10.

29. Tingbin W, Bohong J, Qi X, Liu Y, Xu Dong, Wang Li. Residual stress of TiNi shape memory alloy thin films with (111) single-crystal silicon wafer. Mat Trans. 2002;43(3):566–570.

30. Wang RX, Zohar Y, Wong M. Residual stress-loaded titanium–nickel shape-memory alloy thin-film micro-actuators. J Micromech Microeng. 2002;12(3):323–327.

31. Lehnert T, Crevoiserat S, Gotthardt R. Transformation properties and microstructure of sputter-deposited Ni-Ti shape memory alloy thin films. J Mat Sci. 2002;37:1523–1533.

32. Zhang X, Wu Y, Miao X, Zhang C, Ding G. An electro-thermal SU-8 cantilever micro actuator based on bimorph effect. In: Proceedings of the 2010 5th IEEE International Conference on Nano/Micro Engineered and Molecular Systems; Xiamen, China; 2010. pp. 362–365.

33. Roch I, Bidaud P, Collard D, Buchaillot L. Fabrication and characterization of an SU-8 gripper actuated by a shape memory alloy thin film. J Micromech Microeng. 2003;13:330–336.

34. Knick, CR, Smith GL, Morris CJ, Bruck HA. Rapid and low power laser actuation of sputter-deposited NiTi shape memory alloy (SMA) MEMS thermal bimorph actuators. Sens Act A: Phy. 2019;291:48–57.

35. Knick CR, Sharar DJ, Wilson AA, Smith GL, Morris CJ, Bruck HA. High frequency, low power, electrically actuated shape memory alloy MEMS bimorph thermal actuators. J Micromech Microeng. 2019;29(7):075005.

36. Knick CR, Morris CJ, Smith GL. Rapid and low power laser actuation of sputter-deposited NiTi shape memory alloy (SMA) MEMS thermal bimorph actuators. Sens Act A: Phy. 2019;291:48–57.

37. Mukesh KS, Lakshmi MV. Applications of shape memory alloys in MEMS devices. Int J Adv Res Comp Comm Eng. 2013;2.

38. Dahmardeh M, Mohamed Ali MS, Saleh T, Hian TM, Moghaddam MV, Nojeh A, Takahata K. High-power MEMS switch enabled by carbon-nanotube contact and shape-memory-alloy actuator. Phys Status Solidi A. 2013;210(4):631–638.

39. Namazu T, Tashiro Y, Inoue S. Ti–Ni shape memory alloy film-actuated microstructures for a MEMS probe card. J Micromech Microeng. 2007;17:154–162.

40. Grummon DS, Gotthardt R, LaGrange T. Planar extrinsic biasing of thin film shape-memory MEMS actuators. Mat Res Soc Symp. 2003;741.

41. Xu D, Cai B, Ding G, Zhou Y, Yu A, Wang Li, Zhao X. Novel micropump actuated by thin film shape memory alloy. In: Bergmann NW, Reinhold O, Tien NC, editors. Proceedings of the SPIE, Volume 3891; 1999. pp. 369–375.

42. Wolf RH, Heuer AH. TiNi (shape memory) films on silicon for MEMS applications. J Microelectromech Sys. 1995;4(4):206–212.

43. Fallon PD, Gerratt AP, Kierstead BP, White RD. Shape memory alloy and elastomer composite MEMS actuators. TechConnect Briefs. 2008;3:470–473.

44. Cole DP, Jin H, Lu WY, Roytburd AL, Bruck HA. Reversible nanoscale deformation in compositionally graded shape memory alloy films. App Phys Lett. 2009;94(19):193114.

45. Cole DP, Bruck HA, Roytburd AL. Nanoindentation studies of graded shape memory alloy thin films processed using diffusion modification. J App Phys. 2008;103(6):064315-1–064315-4.

46. Motamedi ME, editor. MOEMS: micro-opto-electro-mechanical systems. Bellingham (WA): SPIE Press; 2005.

47. Klein CA, Miller RP. Strains and stresses in multilayered elastic structures: the case of chemically vapor-deposited ZnS/ZnSe laminates. J Appl Phys. 2000; 87(5):2265–2272.

Appendix. MATLAB Code to Generate Contour Plots

Curvature_ContourPlot.m × Optimization_SMA_bimorph.m* ×

```matlab
clear
close all
clc
% Experimental data
t_NiTi = 1e-9*[100;200;300;400;500;600;700;800;900;1000;1100;1200;1300;1400;1500;1600;1700;1800;1900;2
sigma_rec = 1e6*[0;100;300;400;500;580;590;595;600;570;520;500;480;460;440;430;425;420;410;400;390;380

% Determine polynomial coefficients for curve fitting
coef = polyfit(t_NiTi,sigma_rec,6);
sigma_rec_fitted = polyval(coef,t_NiTi);

figure(1)
plot(t_NiTi*1e9,sigma_rec*1e-6,'o','LineWidth',2)
hold on
plot(t_NiTi*1e9,sigma_rec_fitted*1e-6,'LineWidth',3)
legend('data','fitted curve')
axis([0 4000 0 700])
xlabel('t_{NiTi}, [nm]')
ylabel('\sigma_{rec}, [MPa]')
title('Recovery stress vs NiTi film thickness')
grid on

E_NiTi = 80e9;                % Young's modulus of NiTi layer, [Pa]
E_SU8 = 3e9;                 % Young's modulus of SU8 layer, [Pa]
sigma = 0;                    % Recovery stress, [Pa]

t_NiTi_fitted = ((150:1:1000)*1e-9)';  % NiTi layer thickness, [m]
t_SU8 = ((200:1:2000)*1e-9)';   % SU8 layer thickness, [m]

L = 30e-6;                   % Length of the bimorph, [m]

d = zeros((size(t_NiTi_fitted,1)),(size(t_SU8,1)));

for i = 1:(size(t_NiTi_fitted,1))
    for j = 1:(size(t_SU8,1))
        sigma = coef(1)*t_NiTi_fitted(i)^6+coef(2)*t_NiTi_fitted(i)^5+...
        coef(3)*t_NiTi_fitted(i)^4+coef(4)*t_NiTi_fitted(i)^3+...
        coef(5)*t_NiTi_fitted(i)^2+coef(6)*t_NiTi_fitted(i)+coef(7);
        d(i,j) = (3*E_NiTi*sigma*t_NiTi_fitted(i)*t_SU8(j)*(t_NiTi_fitted(i)+t_SU8(j))*L^2)/...
            (E_NiTi^2*t_NiTi_fitted(i)^4+E_SU8*E_NiTi*(4*t_NiTi_fitted(i)^3*t_SU8(j)+...
            6*t_NiTi_fitted(i)^2*t_SU8(j)^2+4*t_NiTi_fitted(i)*t_SU8(j)^3)+E_SU8^2*t_SU8(j)^4);
    end
end

figure(2)
contourf(t_NiTi_fitted*1e9,t_SU8*1e9,d','LevelStep',1e-5,'LineStyle','none')
colormap jet
colorbar
title('Deflection, l=300 \mum [m]')
xlabel('t_{NiTi}, [nm]')
ylabel('t_{SU8}, [nm]')
```

Fig. A-1 MATLAB script for generation of contour plot for objective Function 1 (deflection)

FILE EDIT NAVIGATE BREAKPOINTS RUN

Curvature_ContourPlot.m

```
clear
close all
clc
E_NiTi = 80e9;                      % Young's modulus of NiTi layer, [Pa]
E_SU8 = 2e9;                        % Young's modulus of SU8 layer, [Pa]
mu_NiTi = 0.33;                     % Poission's ratio of NiTi layer
mu_SU8 = 0.22;                      % Poission's ratio of SU8 layer
Ep_NiTi = E_NiTi/(1-mu_NiTi);       % Biaxial modulus of NiTi layer, [Pa]
Ep_SU8 = E_SU8/(1-mu_SU8);          % Biaxia modulus of SU8 layer, [Pa]
a_NiTi = 9e-6;
a_SU8 = 52e-6;

t_NiTi = ((150:1:1300)*1e-9)';      % NiTi layer thickness, [m]
t_SU8 = ((200:1:2000)*1e-9)';       % SU8 layer thickness, [m]

dT = 200;                           % Temperature Difference
de = dT*(a_SU8-a_NiTi);             % Strain differential term

% Deflection
K = zeros((size(t_NiTi,1)),(size(t_SU8,1)));  % Curvature
rho = zeros((size(t_NiTi,1)),(size(t_SU8,1)));  % Radius Curvature
theta = zeros((size(t_NiTi,1)),(size(t_SU8,1))); % Correction factor
G = zeros((size(t_NiTi,1)),(size(t_SU8,1)));

for i = 1:(size(t_NiTi,1))
    for j = 1:(size(t_SU8,1))
        theta(i,j) = t_NiTi(i)*t_SU8(j)*(Ep_NiTi-Ep_SU8)/...
            (2*(Ep_SU8*t_SU8(j)+Ep_NiTi*t_NiTi(i)));
        G(i,j) = Ep_SU8*t_SU8(j)^2*(t_NiTi(i)/2-t_SU8(j)/6-theta(i,j))-...
         Ep_NiTi*t_NiTi(i)*(t_SU8(j)*(t_SU8(j)+t_NiTi(i)/2)+t_NiTi(i)^2/6+...
         theta(i,j)*(2*t_SU8(j)+t_NiTi(i)));
        K(i,j) = -Ep_SU8*t_SU8(j)*Ep_NiTi*t_NiTi(i)*(t_NiTi(i)+t_SU8(j))/...
            (G(i,j)*(Ep_SU8*t_SU8(j)+Ep_NiTi*t_NiTi(i)))*de;
        rho(i,j) = 1/K(i,j);
    end
end

figure(1)
contourf(t_NiTi*1e9,t_SU8*1e9,rho','LevelStep',1e-4,'LineStyle','none')
colormap jet
colorbar
title('Radius Curvature, [m]')
xlabel('t_{NiTi}, [nm]')
ylabel('t_{SU8}, [nm]')
```

Fig. A-2 MATLAB script for generation of contour plot for objective Function 2 (curvature)

List of Symbols, Abbreviations, Acronyms, and Nomenclature

CTE	coefficient of thermal expansion
MEMS	microelectromechanical system
NiTi	nickel–titanium alloy
Si	silicon
SMA	shape memory alloy
XeF_2	xenon difluoride
bimorph	composite cantilever beam consisting of two materials with different Young's modulus and thickness
α_{NiTi}	CTE of NiTi layer
α_{SU8}	CTE of SU-8 layer
d	deflection of the *SMA MEMS* actuator (micrometer)
E_{NiTi}	elastic modulus of *NiTi* layer (GPa)
E_{SU8}	elastic modulus of *SU-8* layer (GPa)
E'_{NiTi}	biaxial elastic modulus of *NiTi* layer (GPa)
E'_{SU8}	biaxial elastic modulus of *SU-8* layer (GPa)
$\Delta\varepsilon$	strain differential arising from thermal processing and CTE mismatch
l	total length of the *SMA MEMS* actuator (micrometer)
ρ	curvature radius
σ_{rec}	recovery stress of the *SMA MEMS* actuator (MPa)
T_{NiTi}	thickness modulus of *NiTi* layer (nm)
T_{SU8}	thickness modulus of *SU-8* layer (nm)
θ	correction factor term for location of neutral axis

1 (PDF)	DEFENSE TECHNICAL INFORMATION CTR DTIC OCA
1 (PDF)	CCDC ARL FCDD RLD CL TECH LIB
14 (PDF)	CCDC ARL FCDD RLS RL C KNICK C MORRIS R KNIGHT M DUBEY G SMITH D SHARAR A WILSON A LEFF W CHURAMAN R RUDY J PULSKAMP A MOTT N GUPTA B HOFFMAN